Control Engineering Practice 100 (2020) 104442

Contents lists available at ScienceDirect

Control Engineering Practice

journal homepage: www.elsevier.com/locate/conengprac

Energy optimal control of an over-actuated hybrid feed drive under variable-frequency disturbances — with application to machining

Molong Duan *, Keval S. Ramani, Chinedum E. Okwudire

Department of Mechanical Engineering, University of Michigan, 2350 Hayward, Ann Arbor, MI 48109, United States of America

ARTICLE INFO

Keywords:
Energy efficiency
Control allocation
Gain scheduling
Machining
Feed drive

ABSTRACT

Machine tool feed drives are often subject to variable-frequency disturbance (cutting) forces due to varying spindle speeds or cutting tools. A proxy-based control allocation method has been proposed for energy optimal control of over-actuated systems (i.e., systems with more actuators than the number of outputs to be controlled). It has been applied to an over-actuated hybrid feed drive, consisting of a linear motor drive coupled to a screw drive, and its effectiveness has been demonstrated under fixed-frequency disturbance forces. This paper discusses the fundamental limit of the fixed-frequency approach and extends the proxy-based control allocation method to account for variable-frequency disturbance forces via a linear parameter-varying formulation. The controller gains are optimized using linear matrix inequality and scheduled as a function of disturbance frequency. Significant improvements in energy efficiency are demonstrated in simulations and experiments using the proposed gain-scheduling approach compared to the existing fixed-frequency approach.

1. Introduction

There is a growing appreciation of the need to reduce the energy consumption of machine tools without unduly sacrificing quality and productivity (Duflou et al., 2012; Helu et al., 2012). Feed drives are responsible for coordinated motion delivery in machine tools. Hence, they play a critical role in the quality and productivity of machining processes (Altintas et al., 2011); but they also account for a significant portion of machine tool energy consumption (Vijayaraghavan & Dornfeld, 2010), especially when they are driven by linear motors. Among the research on energy consumption reduction of machine tools, energy efficiency enhancement of feed drive is an important topic. Many of the energy efficiency enhancement approaches focus on optimized trajectories, controllers, or workpiece locations. For example, Mori et al. (2011) reduced energy consumption, in part, by synchronizing spindle and feed drive motions. Denkena, Hesse, and Gümmer (2009) proposed an energy optimal design of jerk-decoupled feed axes. Mohammad, Uchiyama, and Sano (2015) and Farrage and Uchiyama (2018) reduced the energy consumption of the feed drive by enhancing the settling performance through sliding mode controllers. Wang et al. (2018) proposed a cloud-based energy-efficient approach in the context of robotic manufacturing. Sato, Shirase, and Hayashi (2018) investigated the optimization of workpiece locations for energy efficiency. These optimization techniques reduce energy consumption but are usually limited by the hardware. Therefore, redundant actuation is increasingly used to further enhance energy efficiency. Halevi, Carpanzano, and Montalbano (2014) proposed minimum energy control of a redundantly actuated feed drive. Du, Plummer, and Johnston (2017) developed an energy-efficient control method for an electrical-hydraulic hybrid motion control system. Okwudire and Rodgers (2013) proposed a hybrid feed drive (HFD), consisting of a linear motor drive (LMD) and a traction screw drive (SD). The HFD is shown in cutting tests to achieve similar positioning precision as an equivalent LMD with up to 80% higher efficiency (Kale, Dancholvi, & Okwudire, 2014).

The HFD is an over-actuated system, i.e., it has more actuators than the number of outputs to be controlled. Over-actuation is often adopted in feed drive systems, and the synergistic cooperation among the redundant actuators is the core control focus (Altintas & Sencer, 2010; Halevi et al., 2014; Schmidt et al., 2017). In the HFD, the primary control objective is to determine an optimal combination of LMD and SD efforts to achieve a desired level of positioning precision using the least control energy from both actuators. Existing control allocation methods (i.e., methods for optimally distributing control efforts) are either computationally expensive or involve approximations that deteriorate positioning precision when applied to over-actuated systems like the HFD (Duan & Okwudire, 2018). Recently, Duan and Okwudire have developed a new approach called proxy-based control allocation (PBCA) for dual-input (Duan & Okwudire, 2018) and multi-input (Duan & Okwudire, 2017) over-actuated systems, and have analyzed its relationship to linear quadratic control (Duan & Okwudire, 2019). The PBCA method converts the control allocation problem for a redundant system to a standard regulation problem of a derived control energy proxy, thus enabling computationally inexpensive control allocation without

* Corresponding author.
E-mail address: molong@umich.edu (M. Duan).

https://doi.org/10.1016/j.conengprac.2020.104442
Received 19 September 2019; Received in revised form 24 April 2020; Accepted 28 April 2020
Available online 15 May 2020

deteriorating positioning performance. The effectiveness of PBCA was demonstrated on the HFD, where up to 95% improvement in efficiency was achieved without sacrificing positioning performance. However, a major drawback of the work presented in Duan and Okwudire (2018) is that, in employing the PBCA, the dominant disturbance frequencies were assumed to be fixed. However, in machining processes, disturbance frequencies change regularly, e.g., due to changing spindle speed or cutting tools with differing number of flutes. Therefore, the primary contributions of this paper are in:

(1) Analytically demonstrating the fundamental limitations of the fixed-frequency PBCA approach by converting the fixed-frequency PBCA design problem into a tracking control problem of a non-minimum phase system.
(2) Proposing a variable-frequency PBCA approach where the parameters of the PBCA are varied (scheduled) as a function of disturbance frequencies, allowing the allocator to change its behavior considering the process information.

The proposed variable-frequency PBCA is compared to the fixed-frequency PBCA (Duan & Okwudire, 2018) in simulations and machining experiments, and large improvements in energy efficiency are demonstrated. The rest of this paper is organized as follows. Section 2 gives an overview of the HFD and the PBCA method. Section 3 analytically demonstrates the fundamental limit of the fixed-frequency PBCA method and formulates the proposed variable-frequency PBCA approach. Section 4 presents the simulation and experimental results, followed by the conclusions and future work in Section 5.

2. Overview of HFD and proxy-based control allocation

2.1. Hybrid feed drive (HFD)

Fig. 1(a) shows the schematic of an HFD prototype whose design is detailed in Okwudire and Rodgers (2013). It consists of an LMD directly connected to the moving table, and a traction SD which can be connected to or disconnected from the table using a (dis)engagement mechanism and twist-roller friction drives. The LMD alone drives the table during rapid traverse motions (while the SD is disengaged from the table). However, during machining, the LMD and SD both actuate the table in parallel (i.e., they act in hybrid mode) to deliver similar positioning precision as the LMD at much higher efficiency (Kale et al., 2014).

During the hybrid mode, the HFD can be modeled as a standard two-mass system (see Fig. 1(b)). In the figure, m_1 and m_2 are the (equivalent) masses of the rotating and translating components of the HFD, while k and c represent the stiffness and viscous damping coefficient of the connecting mechanical components; x_1, x_2, and b_1, b_2 are the (equivalent) displacements and viscous damping coefficients at m_1 and m_2, respectively; u_1 and u_2 are the (equivalent) control forces applied by the rotary and linear motors, while d_1 and d_2 represent external disturbance forces (e.g., non-viscous friction and cutting forces) applied to m_1 and m_2, respectively. Note that $d_1 = 0$ can be assumed because the bearing friction at the rotary motor can be readily determined and compensated in feedforward; therefore, the only (dominant) disturbance considered in this paper is the one acting on the table due to cutting forces (denoted as $d_2 = d$). Defining s as the Laplace variable, the transfer function matrix of the HFD, $\mathbf{G}$, between the input forces (i.e., $\mathbf{u} = \{u_1, u_2\}^{\mathrm{T}}$ and d) and the output displacements (i.e., $\mathbf{x} = \{x_1, x_2\}^{\mathrm{T}}$) is derived as (Duan & Okwudire, 2016)

$$y = x_2 = \underbrace{\begin{bmatrix} G_1 & G_2 \end{bmatrix}}_{\mathbf{G}} \begin{bmatrix} u_1 & u_2 + d \end{bmatrix}^{\mathrm{T}}, \tag{1}$$

where

$$\begin{aligned} &G_1 = \frac{G_{1n}}{D} = \frac{cs+k}{D};\ G_2 = \frac{G_{2n}}{D} = \frac{m_1 s^2 + (c+b_1)s + k}{D};\\ &D = a_4 s^4 + a_3 s^3 + a_2 s^2 + a_1 s;\\ &a_4 = m_1 m_2;\ a_3 = b_1 m_2 + b_2 m_1 + c(m_1 + m_2);\\ &a_2 = c(b_1 + b_2) + k(m_1 + m_2) + b_1 b_2;\ a_1 = (b_1 + b_2)k. \end{aligned} \tag{2}$$

2.2. Proxy-based control allocation method

The overall energy comsumption of feed drive systems is typically analyzed considering the kinetic energy, the cutting energy, and the heat loss (Halevi et al., 2014; Kale et al., 2014). The kinetic energy and the cutting energy depend on the motion trajectory and cutting conditions. The control allocation considered in this paper does not alter the motion trajectory nor the cutting conditions employed. Therefore, the heat loss is selected to be the energy efficiency metric to be minimized. The formulation of heat loss also agrees with the minimum energy control (minimization of two norm of control actions) defined in the control literature (Skogestad & Postlethwaite, 2007). For the HFD, this objective is defined as in (Duan & Okwudire, 2016)

$$E_{heat} = \underbrace{\int \left(\frac{u_1(t)}{K_{m1}}\right)^2 dt}_{E_{heat,1}} + \underbrace{\int \left(\frac{u_2(t)}{K_{m2}}\right)^2 dt}_{E_{heat,2}}. \tag{3}$$

The parameter K_{mi} represents the (equivalent) motor constant of the ith actuator ($i = 1, 2$); it is often reported in the specification sheets of electric motors. The larger the motor constant, the more efficient the motor (see Duan & Okwudire, 2018 for more details). To best utilize the HFD in hybrid mode, optimal combination of u_1 and u_2 that minimizes E_{heat} without sacrificing the positioning accuracy is desired. From Eq. (1), all possible control inputs (i.e., $\mathbf{u}$) that yield the same table position x_2 under specific disturbance signal d satisfy

$$x_2 = G_1 u_1 + G_2(u_2 + d) \Rightarrow G_1 \delta u_1 + G_2 \delta u_2 = 0, \tag{4}$$

where δ represents the variational operator. Note that $\delta d = \delta x_2 = 0$ because they are each fixed, though unknown, functions of time. Also, the most efficient control inputs must minimize E_{heat}; i.e.,

$$\delta\left(\int \left(\left(\frac{u_1}{K_{m1}}\right)^2 + \left(\frac{u_2}{K_{m2}}\right)^2\right) dt\right) = 0 \Rightarrow \frac{u_1}{K_{m1}^2}\delta u_1 + \frac{u_2}{K_{m2}^2}\delta u_2 = 0. \tag{5}$$

Combining Eqs. (4) and (5),

$$\frac{u_1}{u_2} = \beta^*; \qquad \beta \triangleq \kappa^2 \frac{G_1}{G_2}, \tag{6}$$

where $\kappa = K_{m1}/K_{m2}$. The implication of Eq. (6) is that to satisfy a given x_2 requirement at maximum efficiency, the control inputs are bound by an optimal transfer function relationship given by β^*. Note that * represents the adjoint operation, which makes β^* non-causal, meaning that it cannot be evaluated in real time (Duan & Okwudire, 2018). To force u_1 and u_2 to obey the optimal relationship in real time, β^* is decomposed as

$$\beta^* = \frac{\beta_1}{\beta_2} = \left(\underbrace{\frac{R_{22}G_{1n}^* - R_{12}G_{2n}^*}{\psi}}_{\triangleq \beta_1}\right)\left(\underbrace{\frac{R_{11}G_{2n}^* - R_{12}G_{1n}^*}{\psi}}_{\triangleq \beta_2}\right)^{-1}, \tag{7}$$

and a proxy variable u_D is defined as

$$u_D = \beta_2 u_1 - \beta_1 u_2, \tag{8}$$

where β_1 and β_2 are causal transfer functions that can be readily determined using a process detailed in Duan and Okwudire (2018). This concept of control alignment can also be used to estimate the energy performance of an arbitrary controller, this alignment-based energy evaluation is detailed in Duan and Okwudire (2019).

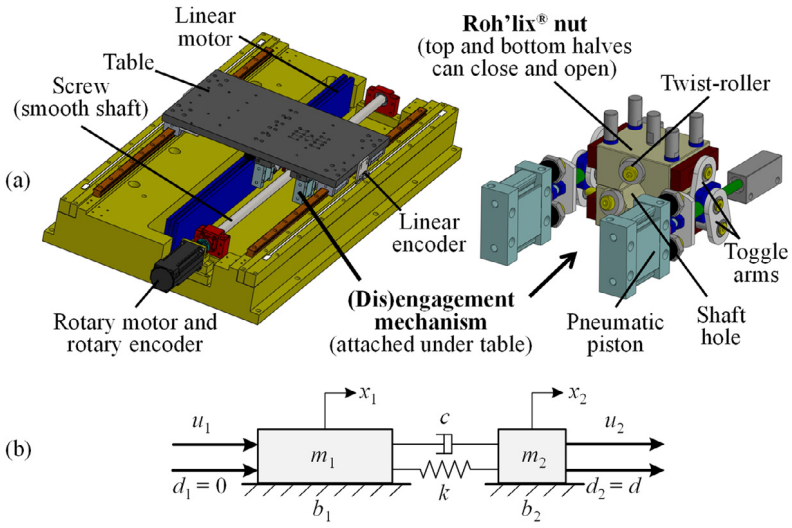

Fig. 1. Schematic of (a) HFD prototype, and (b) two-mass model of HFD.

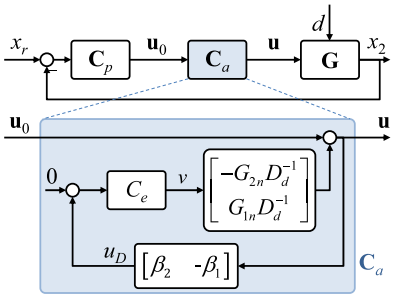

Fig. 2. Block diagram of the two-stage control framework using PBCA.

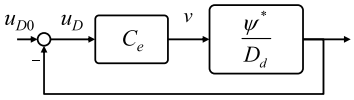

Fig. 3. Analogy to tracking controller design for the NMP system.

Notice that $u_D = 0$ implies that $u_1/u_2 = \beta^*$. Moreover, as $u_D \to 0$, E_{heat} monotonically approaches its minimum value (Duan & Okwudire, 2018). In other words, the variable u_D is a proxy for how far the system is from its optimal efficiency. The farther from 0 the value of u_D gets, the less efficient it becomes (Duan & Okwudire, 2018). This means that energy optimal control of the HFD can be achieved using a two-stage framework as shown in Fig. 2. In Stage 1, a controller $\mathbf{C}_p$ is designed to determine $\mathbf{u}_0 = \{u_{0,1}, u_{0,2}\}^{\mathrm{T}}$ that forces x_2 to track reference position, x_r. A very straightforward way to design such a controller is to use only one control input (i.e., assuming $u_{0,1} = 0$ or $u_{0,2} = 0$), and design a single-input, single-output (SISO) controller to control x_2 using the non-zero input. In Stage 2, a control allocator, $\mathbf{C}_a$, is designed to distribute $\mathbf{u}_0$ optimally to yield $\mathbf{u}$. As shown in the expanded view of $\mathbf{C}_a$, energy optimal allocation is achieved by altering u_D from its initial value of $u_{D0} = \beta_2 u_{0,1} - \beta_1 u_{0,2}$ to $u_D \to 0$ (approaching optimal efficiency). This can be achieved using a standard SISO controller, C_e. Notice from Fig. 2 that $\mathbf{u}$ is forced to satisfy the relationship

$$\mathbf{u} = \mathbf{u}_0 + \begin{bmatrix} -G_{2n}D_d^{-1} \\ G_{1n}D_d^{-1} \end{bmatrix} v \Rightarrow \mathbf{G}\mathbf{u} = \mathbf{G}\mathbf{u}_0, \tag{9}$$

where v is the output of C_e, and $D_d(s)$ is a user-specified replacement denominator of original denominator $D(s)$ for allocator bandwidth control (Duan & Okwudire, 2018). This structure in Eq. (9) ensures that x_2 stays the same as was designed in Stage 1, even as $\mathbf{u}$ is adjusted by C_e to minimize u_D. In other words, Eq. (9) specifies a dynamic null space structure for the over-actuated system. Moreover, this framework supports the saturation constraints on the allocated control effort through output–input constraints conversion. The main idea is to convert the saturation limit to a state-dependent limit on the nulls space variable v. This constraints is especially helpful to alleviate the undesirable slip in the friction drive shown in Fig. 1(a); more detail implementation is discussed in Duan and Okwudire (2018).

3. Design of variable-frequency PBCA

3.1. Fundamental limit of time-invariant PBCA design

According to the analysis in Duan and Okwudire (2018), the two norm of u_D represents the deviation from energy optimality and thus should be minimized. However, it is shown in this section that there exists a fundamental limit to the regulation of u_D to the desired value of zero with a time-invariant PBCA controller. This means that $u_D = 0$ is unattainable, and an analytical lower bound is provided.

Consider the denominator ψ, defined as a spectral decomposition recommended in Duan and Okwudire (2018), i.e.,

$$\psi^*\psi = \begin{bmatrix} G_{2n}^* \\ -G_{1n}^* \end{bmatrix}^{\mathrm{T}} \mathbf{R} \begin{bmatrix} G_{2n} \\ -G_{1n} \end{bmatrix}. \tag{10}$$

This definition ensures that the two-norm of u_D strictly measures the deviation from energy optimality. Then it can be derived, from Eqs. (7) and (10), that

$$\beta_1 G_{1n} + \beta_2 G_{2n} = \frac{\begin{bmatrix} G_{2n}^* \\ -G_{1n}^* \end{bmatrix}^{\mathrm{T}} \mathbf{R} \begin{bmatrix} G_{2n} \\ -G_{1n} \end{bmatrix}}{\psi} = \psi^*. \tag{11}$$

According to the definition of u_D in Eq. (8) and the null space structure in Eq. (9), the control proxy before and after the allocation (u_{D0} and u_D) satisfy the relationship

$$u_D = u_{D0} - \frac{\beta_1 G_{1n} + \beta_2 G_{2n}}{D_d} v = u_{D0} - \frac{\psi^*}{D_d} v. \tag{12}$$

Accordingly, as shown in Fig. 3, the design of C_e is identical to the design of a feedback tracking controller for an equivalent plant given by ψ^*/D_d. Note that D_d is designed by the user and is guaranteed to be a stable denominator, while ψ^* contains non-minimum phase (NMP) zeros since ψ is designed to have only minimum phase zeros (Duan &

Okwudire, 2018). Therefore, plant ψ^*/D_d is a stable NMP system. Note that the only possibility that ψ^* does not contain NMP zeros is that $\psi^*\psi$ is a scalar, which corresponds to the trivial scenario where G_{1n} and G_{2n} are both scalars such that inputs u_1 and u_2 cancel each other prior to affecting the dynamics of the states. For an arbitrary linear time-invariant design of C_e, the tracking performance of a stable NMP system has a fundamental limit. According to Chen, Qiu, and Toker (2000), the minimum tracking error of u_D for a step input from u_{D0} is given by

$$\min_{C_e} \int_0^\infty \|u_D(t)\|^2 dt = \sum_i \frac{2\mathrm{Re}(z_i)}{|z_i|^2} \cos^2 \angle(\eta_i, u_{D0}(0^+)), \tag{13}$$

where z_i is the NMP zeros in plant ψ^*/D_d and η_i is the corresponding NMP zero direction vector. In the HFD setup, $\cos^2 \angle(\eta_i, u_{D0}(0^+)) = 1$, since u_{D0} and u_D are scalar signals. According to Eqs. (7) and (11),

$$\psi^* = \frac{m_1 s^2 - a_{\psi 1} s + a_{\psi 0}}{K_{m1}}, \tag{14}$$

where

$$\begin{aligned} a_{\psi 1} &= \sqrt{2m_1 k\sqrt{(1+\gamma)} - 2m_1 k + (c+b_1)^2 + \gamma c^2}, \\ a_{\psi 0} &= k\sqrt{(1+\gamma)}, \end{aligned} \tag{15}$$

and $\gamma = (K_{m,1}/K_{m,2})^2$ represents the energy efficiency ratio between the screw drive and the linear motor drive. Therefore, the minimum value of the expression in Eq. (13) is derived as

$$\min_{C_e} \int_0^\infty \|u_D(t)\|^2 dt = 2\left(\frac{1}{z_1} + \frac{1}{z_2}\right) = \frac{2a_{\psi 1}}{a_{\psi 0}}. \tag{16}$$

This expression provides the fundamental limit on the time-invariant C_e design for the HFD in the time domain for a representative step input. In the frequency domain, since the analogous plant ψ^*/D_d is stable with NMP zeros, the fundamental limit can be interpreted using the weighted Bode's sensitivity integral formula (Skogestad & Postlethwaite, 2007), i.e.,

$$\int_0^\infty \ln\left|\frac{u_D(j\omega)}{u_{D0}(j\omega)}\right| \cdot w(z_1, z_2, \omega)\, d\omega = 0, \tag{17}$$

where $w(z_1, z_2, \omega)$ is a weighting function given by

$$\begin{aligned} w(z_1, z_2, \omega) &= \sum_{i=1,2} \frac{\mathrm{Re}(z_i)}{\mathrm{Re}(z_i)^2 + (\mathrm{Im}(z_i) - \omega)^2} \\ &= \frac{a_{\psi 1}(a_{\psi 0} + \omega^2)}{\omega^4 - \left(4a_{\psi 1}^2 - 18a_{\psi 0}\right)\omega^2 + a_{\psi 0}^2}. \end{aligned} \tag{18}$$

Note that $w(z_1, z_2, \omega)$ is positive for all $\omega>0$, and reaches its maximum when $\omega \approx |\mathrm{Im}(z_1)|$. This illustrates that the sensitivity of the waterbed effect is especially high around the NMP zero frequencies. This fundamental limit indicates that $u_D = 0$ is not achievable across a wide range of disturbance frequencies due to the heightened waterbed effect caused by the NMP zeros in plant ψ^*/D_d, i.e., a time-invariant C_e designed to regulate u_D over a wide frequency band would have very limited effectiveness.

3.2. PBCA designs considering variable disturbance frequencies

Information from the reference trajectory and the cutting disturbances can be used to facilitate more effective regulation u_{D0} despite the fundamental limit of the PBCA design derived in the preceding section. Based on Fig. 3 and Eq. (12), the relationship between u_D and u_{D0} can be expressed as

$$u_D = \frac{1}{1 + C_e \frac{\psi^*}{D_d}} u_{D0}. \tag{19}$$

It has been analyzed in Section 3.1 that $u_D = 0$ cannot be achieved over a wide range of disturbance frequencies with time-invariant C_e design due to the fundamental limitation of tracking accuracy in Eq. (16) and waterbed effect specified in Eq. (17). However, C_e can be designed to regulate u_{D0} at its dominant frequencies to maximize the overall energy efficiency (to reduce heat loss). As Fig. 2 indicates, u_{D0} can be treated as the output of the reference x_r and cutting force d. Due to linear property, dominant frequency components in x_r and d are carried into u_{D0}. From these two sources, the disturbance force d is dominant during cutting since the motion is usually scheduled at constant or very smooth velocity (i.e., the dynamic components in x_r are less dominant than those in d). The cutting force d is usually periodic in the time domain, resulting in its frequency components to be concentrated at zero frequency and discrete finite frequencies f_j ($j = 0, 1, 2, \ldots, N-1$). Accordingly, C_e can be designed, using the internal model principle (Duan & Okwudire, 2018), as

$$C_e(s) = K_e \frac{1}{s+\varepsilon} \prod_{j=0}^{N-1} \frac{\omega_j^2}{s^2 + 2\zeta_j \omega_j s + \omega_j^2} H_{LP}(s), \tag{20}$$

where K_e is the controller gain, and the next two terms provide high gains at zero frequency and at frequencies $\omega_j = 2\pi f_j$, respectively, if ε and ζ_j are selected to be very small numbers. Note that ζ_j changes the width of the peak around frequency ω_j, therefore it should be kept sufficiently large when there is uncertainty in ω_j. According to the 3 dB rule in modal analysis (Inman, 2014), ζ_j should be larger than $|\Delta\omega_j|/(2\omega_j)$ to guarantee robustness, where $\Delta\omega_j$ represent the uncertainty of disturbance frequency ω_j. Transfer function $H_{LP}(s)$ is a low-pass filter used to attenuate higher frequency content from d and ensure stability. Note from Eq. (19) that larger K_e values lead to smaller u_D, and the high resonant peak at ω_j guarantees large $|C_e(j\omega_j)|$, resulting in a very small spectrum component of u_D at this frequency. The assumption implied in Eq. (20) is that the dominant frequencies of d are invariant (fixed). However, in most practical machining scenarios, the dominant frequencies can change with the change of spindle speed and cutting tools. Therefore, a design of C_e considering the variable frequency of the cutting disturbance is necessary.

For this purpose, the dominant frequency ω_j is relaxed to be a time-varying parameter, denoted as $\omega_j(t)$. Here it is assumed that the time trace of $\omega_j(t)$ is known a priori (i.e., the change of frequency can happen at arbitrary time instant during the cutting operation and is known to the controller). It is assumed that the rate of frequency variation is significantly slower compared to the feed drive control bandwidth. Moreover, the change in frequency can be continuous or discrete. These assumptions are usually satisfied in practical machining scenarios. This frequency-based scheduling is also employed in screw drive control where the resonant frequency is position-dependent (Hanifzadegan & Nagamune, 2013). With $\omega_j(t)$, C_e in Eq. (20) becomes a transfer function with time-varying coefficients. It is realized using its controllable canonical state–space realization such that the parameterized state–space matrices are guaranteed to be continuous with respect to varying parameter $\omega_j(t)$. Consider also the state–space representation of other linear time-invariant components in Fig. 3, the closed-loop system from u_{D0} to u_D is represented by the following linear parameter varying system:

$$\begin{aligned} \dot{\mathbf{x}}_c(t) &= \mathbf{A}_c(\omega_j(t))\mathbf{x}_c(t) + \mathbf{B}_c(\omega_j(t))u_{D0}(t) \\ u_D(t) &= \mathbf{C}_c(\omega_j(t))\mathbf{x}_c(t) + D_c(\omega_j(t))u_{D0}(t), \end{aligned} \tag{21}$$

where $\mathbf{x}_c(t)$, $\mathbf{A}_c(\omega_j(t))$, $\mathbf{B}_c(\omega_j(t))$, $\mathbf{C}_c(\omega_j(t))$, and $D_c(\omega_j(t))$ are the state vector, state matrix, input matrix, output matrix, and feedthrough term, respectively. This state–space realization uses observable canonical form such that the physical meanings of the states at different ω_j are consistent. Note that the changing parameter does not change the system order such that the size of $\mathbf{A}_c$, $\mathbf{B}_c$, $\mathbf{C}_c$, and D_c are consistent for different ω_j. The state matrix can be expressed using an affine parameter-dependent model (Symens, van Brussel, & Swevers, 2004)

$$\mathbf{A}_c(\omega_j(t)) = \mathbf{A}_0 + \sum_{i=1}^{M} \rho_i(\omega_j(t))\mathbf{A}_i, \tag{22}$$

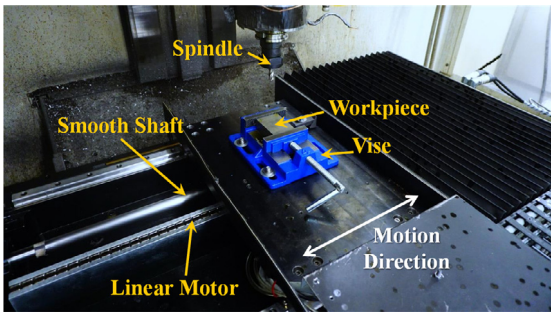

Fig. 4. Experiment setup: HFD mounted on a milling machine.

where $\rho_i(\omega_j(t)) \in [-1,1]$, $\mathbf{A}_0$ and $\mathbf{A}_i$ are constant matrices, and M is the order (number of states) of the system. The system described by Eqs. (21) and (22) is stable if there exists matrices $\mathbf{P} > 0$ and $\mathbf{X}_i$ $(i = 1, 2, \ldots, M)$ such that the following linear matrix inequalities (LMIs) hold (Briat, 2014)

$$-\mathbf{X}_i \pm \left(\mathbf{A}_i^{\mathrm{T}}\mathbf{P} + \mathbf{P}\mathbf{A}_i\right) \leq 0;\ \mathbf{A}_0^{\mathrm{T}}\mathbf{P} + \mathbf{P}\mathbf{A}_0 + \sum_{i=1}^{M} \mathbf{X}_i < 0, \tag{23}$$

where "> 0" and "< 0" denote the positive and negative definiteness of a matrix, respectively. Note that the satisfaction of Eq. (23) implies the existence of a common quadratic Lyapunov function that guarantees a stable system as controllers are switched rapidly to accommodate arbitrary variations in disturbance frequencies, $\omega_j(t)$. This quadratic stability criterion is used to seek the maximum admissible values of K_e in Eq. (20). The procedure is detailed as follows. The maximal K_e values which guarantee the stability of the individual linear system are firstly calculated. The corresponding affine parameter model in Eq. (22) is then generated and verified for the common Lyapunov function condition in Eq. (23). If the common Lyapunov function is not satisfied, the $K_e(\omega_j)$ values are iteratively reduced until Eq. (23) is satisfied. Note that the linear parameter varying system converges to a common stable linear invariant system when K_e approaches 0, which indicates the feasibility of K_e values for the given LMI conditions in Eq. (23).

4. Simulations and experiments

Simulations and machining experiments are conducted to demonstrate the effectiveness of the proposed variable-frequency (VF) PBCA, compared to the fixed-frequency (FF) PBCA and a baseline case (without control allocation). Fig. 4 shows the set-up used for the experiments, where the HFD is mounted on a FADAL vertical machining center to enable milling at variable spindle speeds. The experimentally identified parameters of the HFD's two-mass model are shown in Table 1. The parameters are acquired by fitting the experimental frequency response function to a two-mass model (Duan & Okwudire, 2018). The (equivalent) motor constants for its rotary and linear motors are $K_{m,1} = 380.8\ \mathrm{N}/\sqrt{\mathrm{W}}$ and $K_{m,2} = 21\ \mathrm{N}/\sqrt{\mathrm{W}}$, respectively. Therefore, $\kappa^2 = (K_{m,1}/K_{m,2})^2 = 328.8$, indicating two orders of magnitude difference in the efficiencies of the two actuators. The cutting disturbance is machining disturbance is assumed to be concentrated at a single frequency given by Jauregui et al. (2018)

$$f_0 = \frac{n_{rpm} n_{flute}}{60}. \tag{24}$$

where n_{rpm} is the spindle speed in round per minute, and n_{flute} is the number of flutes in the milling tool. In simulation, additional biased sinusoidal forces are generated from the linear motor to represent the cutting forces due to this frequency dominance.

Table 1
Experimentally identified parameters of HFD's two-mass model.

m_1 [kg]	m_2 [kg]	b_1 [kg/s]	b_2 [kg/s]	c [kg/s]	k [N/μm]
616.2	46.3	44.8	83.3	5777.2	3.147

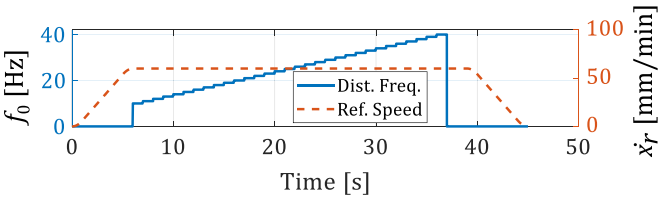

Fig. 5. Table's reference speed ($\dot{x}_r$) and disturbance frequency (f_0) as functions of time.

4.1. Simulations

In simulations, the HFD's table is commanded to travel at a constant speed of 60 mm/min while disturbance $d = A(\cos(2\pi f_0 t) - 1)$ N is applied to it, with $A = 100$ N and f_0 varying from 10 to 40 Hz in 1 Hz increments, as shown in Fig. 5. The following controller cases are considered.

4.1.1. Baseline case (no control allocation)

In Fig. 2, $\mathbf{C}_a = \mathbf{I}$ (identity matrix) is assumed; $\mathbf{C}_p$ is selected as

$$\mathbf{u}_0 = \mathbf{C}_p \underbrace{(x_r - x_2)}_{e_2} = \begin{bmatrix} 0 & K_p + \frac{K_i}{s} + \frac{K_d s}{T_f s + 1} \end{bmatrix}^{\mathrm{T}} e_2. \tag{25}$$

The implication is that $\mathbf{C}_p$ is a standard SISO PID controller applied to the LMD; K_p, K_i, and K_d are tuned to 7.46×10^6 N/m, 4.07×10^6 N/m/s and 1.01×10^5 Ns/m, respectively, and the time constant of the stabilizing low-pass filter is set at $T_f = 1.39 \times 10^{-4}$ s.

4.1.2. Fixed-frequency (FF) allocation case

The same $\mathbf{C}_p$ from the baseline case is used. However, for $C_e = C_{e,fixed}$, a PBCA is designed for a fixed frequency $f_0 = 25$ Hz (i.e., the median of 10 to 40 Hz). Referring to Eq. (20) with $N = 1$, $\varepsilon = 10^{-5}$ rad/s and $\zeta = 10^{-2}$ are selected to achieve very high gains at 0 Hz and 25 Hz, respectively; H_{LP} is chosen such that the marginally stable denominator D (see Eq. (2)) is replaced with a stable 6th order Butterworth filter with a cut-off frequency of $f_0 + 10$ Hz. Gain $K_e = 501\ \mathrm{N}/\sqrt{\mathrm{W}}$ is then selected to ensure stability with a gain margin of 6 dB, using standard controller tuning techniques.

4.1.3. Variable-frequency (VF) allocation case

The same $\mathbf{C}_p$ from the baseline case is used. For every discrete value of f_0, i.e., 10, 11, 12, …, 40 Hz, C_e, and H_{LP} are designed in a manner similar to that for FF allocation. However, to ensure that stability is maintained as the gains are scheduled, for each value of f_0, K_e must be chosen such that Eq. (23) is satisfied. To do this, K_e is selected to achieve a 6-dB gain margin at each discrete f_0 based on $C_{e,fixed}$. Next Eq. (19) is converted to state–space form to determine $\mathbf{A}_c$, $\mathbf{B}_c$, $\mathbf{C}_c$, and D_c in (Eq. (21)) for all f_0, based on the determined K_e values. Matrices $\mathbf{A}_0, \mathbf{A}_1, \ldots, \mathbf{A}_M$ (with $M = 9$) are then determined such that $\mathbf{A}_c$ for all f_0 can be represented using the affine parameter-dependent model of Eq. (22). It is found that the condition in Eq. (23) is satisfied. This implies that the K_e value with the 6-dB gain margin for each f_0 guarantee stability as the PBCA is scheduled as a function of f_0. The resulting values of K_e as a function of f_0 is shown in Fig. 6, where there are two drops at low- and high-frequency ranges. The drop in low frequency arises from the $1/(s+\varepsilon)$ term in Eq. (20), while the drop in high frequency arises from the physical limitation of the controllability from the non-collocated rotary motor.

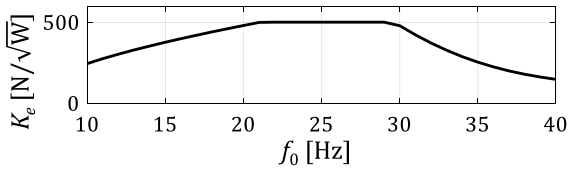

Fig. 6. Gain K_e as a function of f_0 for variable-frequency allocator.

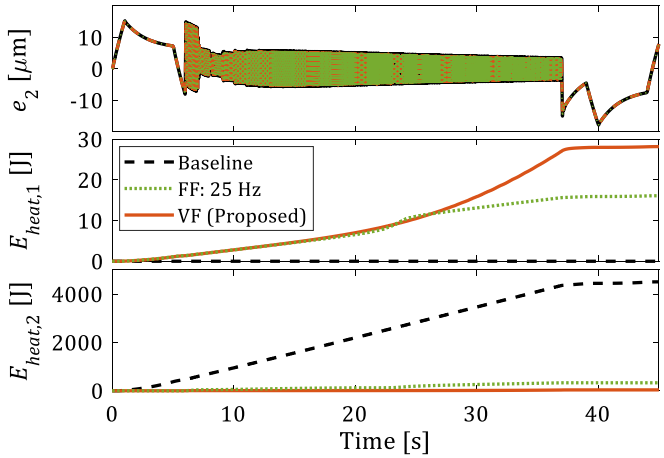

Fig. 7. Simulated positioning error and actuator heat loss using baseline, fixed-frequency, and variable-frequency allocator cases.

Table 2
Simulated positioning error and actuator heat loss using baseline, fixed-frequency, and variable-frequency allocator cases.

	Baseline	FF Allocator @ 25 Hz	VF Allocator
$e_{2,\text{rms}}$ [μm]	6.22	6.22	6.22
$E_{heat,1}$ [J]	0	16.10	28.17
$E_{heat,2}$ [J]	4505.63	330.18	36.85
E_{heat} [J]	4505.63	346.28	65.02

Table 3
Cutting parameters.

Spindle speed (rpm)	300/750/1200
Tool	3/16" dia., 2-fluted, HSS end mill
Workpiece	1018 cold finished mild steel
Feed per tooth (mm/tooth)	0.03/0.012/0.0075
Feed rate (mm/min)	18
Lubrication	None

Fig. 7 shows the simulated table positioning error $e_2 = x_r - x_2$, as well as the resultant $E_{heat,1}$ and $E_{heat,2}$ for the FF and VF allocators, compared with the baseline case (all using the $\dot{x}_r$ and f_0 shown in Fig. 5); Table 2 summarizes the results. Notice that the 6.22 μm RMS positioning error is the same for all three cases. This is because the PBCA method guarantees that control allocation (i.e., Stage 2 of the two-stage process in Fig. 2) does not alter positioning performance determined in Stage 1. The FF allocator uses less the energy-efficient screw drive and thus the for the $E_{heat,1}$ for the FF allocator is less than VF allocator. This insufficient use of the screw drive leads to a significant increase in $E_{heat,2}$. Therefore, although the FF allocator generates 92% less heat compared to the baseline case, the proposed VF allocator generates 81% less heat compared to the FF allocator. The proposed VF allocation approach is significantly more energy efficient compared to the baseline and FF allocator.

4.2. Experiment

Cutting tests are carried out to verify the performance of the proposed VF allocator experimentally. Three 3 mm-long and 2 mm-deep slots are cut at different spindle speeds using cutting parameters reported in Table 3. Note that three discrete spindle speeds (i.e., 300, 750 and 1200 rpm) are used in the experiments because the spindle speed on the machine tool cannot be controlled to vary continuously with the motion of the HFD in a synchronized manner. A two-fluted end mill is used, so 300, 750 and 1200 rpm correspond to dominant cutting frequencies, f_0, at 10, 25 and 40 Hz, respectively.

The three cases discussed in Section 4.1 are compared in the experiments. The only difference between the controllers used in simulations and experiments is that $\mathbf{C}_p$ is changed to

$$\mathbf{u}_0 = \mathbf{C}_p \underbrace{\left(x_r - x_2\right)}_{e_2} = \begin{bmatrix} K_{p,1} + \frac{K_{i,1}}{s} + K_{d,1}s & K_{p,2} + K_{d,2}s \end{bmatrix}^{\mathrm{T}} e_2 \tag{26}$$

with gain values reported in Table 4. Essentially, in Eq. (26), $\mathbf{C}_p$ is made to also control the rotary motor (together with the linear motor) because, due to friction in the Roh'lix nut, the linear motor alone cannot back-drive the rotary motor. For the FF allocator case, $C_{e,fixed}$ designed based on 25 Hz in Section 4.1.2 is used for cutting at the three spindle speeds. Similarly, for the VF allocator, the C_e designed for 10, 25 and 40 Hz in Section 4.1.3 are respectively applied to cutting at 300, 750 and 1200 rpm.

Fig. 8 shows e_2 (measured from the linear encoder) as well as $E_{heat,1}$ and $E_{heat,2}$ (calculated from the motor currents/forces using Eq. (3)) for the baseline (BL), FF allocator and VF allocator cases; the results are summarized in Table 5. Notice that, for each spindle speed, the RMS positioning error is very similar among the three cases, again, due to the properties of the PBCA method. The slight (≤0.5 μm) differences among the errors are due to modeling errors and slight variations in conditions that cannot be completely avoided in experiments. Note that the positioning errors of the 300 rpm tests are a bit higher than those at 750 and 1200 rpm due to higher cutting forces at lower spindle speeds. This higher cutting forces arise from the higher feeds per tooth, which increases with the mean cutting force at the feed direction (Rubeo & Schmitz, 2016). At 1200 rpm, the proposed VF approach generates 59% less heat than the baseline case, while the FF allocator generates 3% more heat than the baseline case because it is not tuned for dominant forces at 1200 rpm. The situation is worse at 300 rpm where the FF allocator generates almost 3 times more heat compared to the baseline case, while the proposed VF allocator generates 63% less heat compared to the baseline case. The results of the FF and VF allocators converge at 750 rpm, and generate both

Table 5
Positioning error and actuator heat loss in cutting experiments using baseline, fixed-frequency, and variable-frequency allocator cases.

	300 rpm			750 rpm			1200 rpm		
	BL	FF	VF	BL	FF	VF	BL	FF	VF
$e_{2,\text{rms}}$ [μm]	2.7	2.4	2.8	1.8	2.0	2.0	2.4	2.5	2.0
$E_{heat,1}$ [J]	4.8	5.3	5.2	4.6	5.6	5.6	10.9	11.2	8.8
$E_{heat,2}$ [J]	27.2	121.4	6.7	14.7	6.1	6.1	32.9	34.0	9.2
E_{heat} [J]	32.0	126.7	11.9	19.4	11.8	11.8	43.8	45.2	18.0
E_{heat} reduction	–	−296%	63%	–	39%	39%	–	−3%	59%

Table 4
Values of $\mathbf{C}_p$ controller gains in Eq. (26).

$K_{p,1}$ [N · m^{-1}]	$K_{i,1}$ [N · m^{-1} · s^{-1}]	$K_{d,1}$ [N · m^{-1} · s]	$K_{p,2}$ [N · m^{-1}]	$K_{d,2}$ [N · m^{-1} · s]
3.1×10^7	4.2×10^8	5.2×10^5	1.1×10^7	3.4×10^4

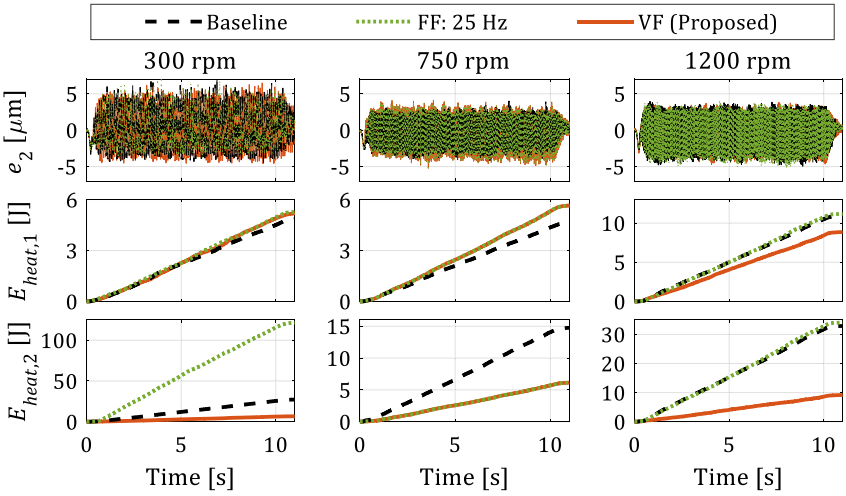

Fig. 8. Positioning error and actuator heat loss in cutting experiments using baseline, fixed- frequency, and variable-frequency allocator cases.

39% less heat compared to the baseline case. The comparison of heat losses clearly illustrates the energy efficiency advantage of VF allocator without sacrificing positioning accuracy.

Note that the simulation and experiment setting use different baseline controllers. The baseline control in the simulation uses only the linear motor drive (u_2) for actuation, which illustrates the performance gain of the adoption of redundant actuation. In experiments, this pure use of linear motor for actuation is not possible since it may mechanically damage the reconfigurable friction drive. Since this baseline controller adopted already has a built-in level of control allocation, the energy performance gain is relatively smaller compared to the simulation results. Also, it is clear that poor control alignment at the disturbance frequency may introduce more energy consumption to the baseline system. In this regard, the fixed frequency approach is not always efficient, the accurate information of the disturbance frequency is necessary for energy efficiency enhancements.

5. Conclusions and future work

The existing practice for designing proxy-based control allocator (PBCA) assumes that the disturbance force frequency is invariant (fixed). However, in machining applications, disturbance (i.e., cutting) force frequencies vary as spindle speed and cutting tools are changed. It is analytically proved that a broad-band PBCA design has fundamental limitations in its effectiveness. To enhance the energy efficiency of machining, a variable-frequency (VF) PBCA is proposed for energy optimal control of an over-actuated hybrid feed drive. The proposed VF allocator accounts for changes disturbance force's frequency by scheduling controller gains as a function of the disturbance force frequencies. The stability of the VF allocator is guaranteed during gain scheduling by selecting its gains to satisfy Lyapunov stability conditions. The proposed VF allocator is compared with the existing fixed-frequency (FF) allocator in simulations and cutting experiments; significant improvements in efficiency are achieved without (significant) sacrifice to positioning precision. Future work will extend the energy optimal control design exploiting more cutting process information beyond the disturbance frequency, dynamic slip compensation in the hybrid feed drive will also be investigated.

Declaration of competing interest

The authors declare that they have no known competing financial interests or personal relationships that could have appeared to influence the work reported in this paper.

Acknowledgment

This work is funded in part by the National Science Foundation's CAREER Award, USA #1350202: Dynamically Adaptive Feed Drives for Smart and Sustainable Manufacturing. The support is greatly appreciated.

References

Altintas, Y., & Sencer, B. (2010). High speed contouring control strategy for five-axis machine tools. *CIRP Annals*, *59*(1), 417–420. http://dx.doi.org/10.1016/j.cirp.2010.03.019.

Altintas, Y., et al. (2011). Machine tool feed drives. *CIRP Annals*, *60*(2), 779–796. http://dx.doi.org/10.1016/j.cirp.2011.05.010.

Briat, C. (2014). *Linear parameter-varying and time-delay systems: Analysis, observation, filtering & control*. Springer.

Chen, J., Qiu, L., & Toker, O. (2000). Limitations on maximal tracking accuracy. *IEEE Transactions on Automatic Control*, *45*(2), 326–331.

Denkena, B., Hesse, P., & Gümmer, O. (2009). Energy optimized jerk-decoupling technology for translatory feed axes. *CIRP Annals*, *58*(1), 339–342. http://dx.doi.org/10.1016/j.cirp.2009.03.043.

Du, C., Plummer, A. R., & Johnston, D. N. (2017). Performance analysis of a new energy-efficient variable supply pressure electro-hydraulic motion control method. *Control Engineering Practice*, *60*, 87–98.

Duan, M., & Okwudire, C. E. (2016). Energy-efficient controller design for a redundantly-actuated hybrid feed drive with application to machining. *IEEE/ASME Transactions on Mechatronics*, *21*(4), 1822–1834. http://dx.doi.org/10.1109/TMECH.2015.2500165.

Duan, M., & Okwudire, C. E. (2017). Proxy-based optimal dynamic control allocation for multi-input, multi-output over-actuated systems. In *Proceedings of the ASME 2017 dynamic systems and control conference*. Tyson, VA: ASME, http://dx.doi.org/10.1115/DSCC2017-5343, p. V001T03A005.

Duan, M., & Okwudire, C. E. (2018). Proxy-based optimal control allocation for dual-input over-actuated systems. *IEEE/ASME Transactions on Mechatronics*, *23*(2), 895–905. http://dx.doi.org/10.1109/TMECH.2018.2796500.

Duan, M., & Okwudire, C. E. (2019). Connections between control allocation and linear quadratic control for weakly redundant systems. *Automatica*, *101*, 96–102. http://dx.doi.org/10.1016/j.automatica.2018.11.049.

Duflou, J. R., et al. (2012). Towards energy and resource efficient manufacturing: A processes and systems approach. *CIRP Annals*, *61*(2), 587–609. http://dx.doi.org/10.1016/j.cirp.2012.05.002.

Farrage, A., & Uchiyama, N. (2018). Energy saving in biaxial feed drive systems using adaptive sliding mode contouring control with a nonlinear sliding surface. In *Mechatronics: Vol. 54*, (pp. 26–35). Elsevier.

Halevi, Y., Carpanzano, E., & Montalbano, G. (2014). Minimum energy control of redundant linear manipulators. *Journal of Dynamic Systems, Measurement and Control*, *136*(5), 051016. http://dx.doi.org/10.1115/1.4027419.

Hanifzadegan, M., & Nagamune, R. (2013). Switching gain-scheduled control design for flexible ball-screw drives. *Journal of Dynamic Systems, Measurement and Control*, *136*(1), 014503. http://dx.doi.org/10.1115/1.4025154.

Helu, M., et al. (2012). Impact of green machining strategies on achieved surface quality. *CIRP Annals*, *61*(1), 55–58. http://dx.doi.org/10.1016/j.cirp.2012.03.092.

Inman, D. J. (2014). *Engineering vibration* (fourth ed.). Pearson Education, Inc.

Jauregui, J. C., et al. (2018). Frequency and time-frequency analysis of cutting force and vibration signals for tool condition monitoring. *IEEE Access*, *6*, 6400–6410.

Kale, S., Dancholvi, N., & Okwudire, C. (2014). Comparative LCA of a linear motor and hybrid feed drive under high cutting loads. *Procedia CIRP*, *55*, 2–557. http://dx.doi.org/10.1016/j.procir.2014.03.055.

Mohammad, A. M. A. E. K, Uchiyama, N., & Sano, S. (2015). Energy saving in feed drive systems using sliding-mode-based contouring control with a nonlinear sliding surface. *IEEE/ASME Transactions on Mechatronics*, *20*(2), 572–579. http://dx.doi.org/10.1109/TMECH.2013.2296698.

Mori, M., et al. (2011). A study on energy efficiency improvement for machine tools. *CIRP Annals*, *60*(1), 145–148. http://dx.doi.org/10.1016/j.cirp.2011.03.099.

Okwudire, C., & Rodgers, J. (2013). Design and control of a novel hybrid feed drive for high performance and energy efficient machining. *CIRP Annals*, *62*(1), 391–394. http://dx.doi.org/10.1016/j.cirp.2013.03.139.

Rubeo, M. A., & Schmitz, T. L. (2016). Milling force modeling: a comparison of two approaches. In *Procedia manufacturing*: *Vol. 5*, (pp. 90–105). Elsevier.

Sato, R., Shirase, K., & Hayashi, A. (2018). Energy consumption of feed drive systems based on workpiece setting position in five-axis machining center. *Journal of Manufacturing Science and Engineering*, *140*(2), 21008.

Schmidt, L., et al. (2017). Position control of an over-actuated direct hydraulic cylinder drive. *Control Engineering Practice*, *64*, 1–14.

Skogestad, S., & Postlethwaite, I. (2007). *Multivariable feedback control: Analysis and design*. Wiley New York.

Symens, W., van Brussel, H., & Swevers, J. (2004). Gain-scheduling control of machine tools with varying structural flexibility. *CIRP Annals*, *53*(1), 321–324. http://dx.doi.org/10.1016/S0007-8506(07)60707-0.

Vijayaraghavan, A., & Dornfeld, D. (2010). Automated energy monitoring of machine tools. *CIRP Annals*, *59*(1), 21–24. http://dx.doi.org/10.1016/j.cirp.2010.03.042.

Wang, L., et al. (2018). Energy-efficient robot applications towards sustainable manufacturing. *International Journal of Computer Integrated Manufacturing*, *31*(8), 692–700.